MIT Libraries | DSpace@MIT

MIT Open Access Articles

Understanding the fundamental driver of semiconductor radiation tolerance with experiment and theory

Massachusetts Institute of Technology

Understanding the fundamental driver of semiconductor radiation tolerance with experiment and theory

Julie V. Logan [1,2,*] Preston T. Webster,[1] Kevin B. Woller,[2] Christian P. Morath,[1] and Michael P. Short [2]

[1]*Air Force Research Laboratory, Space Vehicles Directorate, Kirtland AFB, New Mexico 87117, USA*
[2]*Department of Nuclear Science and Engineering, Massachusetts Institute of Technology,*
77 Massachusetts Ave, Cambridge, Massachusetts 02139, USA

Space is the operating environment of a multitude of systems that our society is heavily reliant on today, however, maintaining operability there necessitates special consideration of the electronic systems' tolerance of space radiation. Electronic systems are critically dependent on the electronic properties of their semiconductor components, which are modified by space radiation with an adverse impact on the space system performance. What innate property allows some semiconductors to sustain little damage while others accumulate defects rapidly with dose is poorly understood, which limits the extent to which radiation tolerance can be implemented as a design criterion. To gain insight into what properties are drivers of semiconductor radiation tolerance, the first step is to generate a dataset of the relative radiation tolerance of a broad sampling of semiconductors. To accomplish this, Rutherford backscatter channeling experiments are used to compare the displaced lattice atom buildup in InAs, InP, GaP, GaN, ZnO, MgO, and Si as a function of stepwise alpha particle dose. With this experimental information on radiation-induced incorporation of interstitial defects in hand, hybrid density functional theory electron densities (and their derived quantities) are calculated and their gradient and Laplacian are evaluated to obtain key fundamental information about the interactions in each material. It is shown that simple, undifferentiated values (which are typically used to describe bond strength) are insufficient to predict radiation tolerance. Instead, the curvature of the electron density at bond critical points provides a measure of radiation tolerance consistent with the experimental results obtained. This curvature and associated forces surrounding bond critical points have the potential to disfavor the localization of displaced lattice atoms at these points, favoring their diffusion toward perfect lattice positions. With this criterion to predict radiation tolerance, simple density functional theory simulations can be conducted on potential new materials to gain insight into how they may operate in demanding high radiation environments.

I. INTRODUCTION

While the ease and wide range over which the electronic properties of semiconductors can be tuned has made them incredibly useful components in electronic systems, this feature becomes detrimental in radiation environments where particle radiation itself may modify the semiconductor's properties, deteriorating the electronic system's performance or disabling it entirely. This includes environments with high fluxes of damaging high-energy particles such as in nuclear reactors, particle accelerators, and in the Earth's magnetosphere. The ionizing dose and displacement damage effects in electronic devices are a significant system failure mechanism, and for this reason, electronic components must be tested for their operation under radiation damage prior to deployment [1]. Society is heavily reliant on the continued operation of satellites, which are themselves heavily reliant on the fidelity of their constituent semiconductors. It has been observed that semiconductors vary dramatically in their radiation tolerance, with HgCdTe being approximately $10\times$ more radiation toler-

ant than III-V materials [2], ZnO being $30\times$ more radiation tolerant than GaN [3], and GaAs being more than $10\times$ more radiation tolerant than Si [4]. However, these comparisons are dependent on the damage mode and metric used to assess material quality [5]. For this reason, in this analysis, the defect content is probed directly rather than through measurement of defect effect on material or device properties.

The question of what fundamentally determines the radiation tolerance of a semiconductor is still open [6,7]. Various metrics have been proposed to correlate with radiation tolerance (bond strength, ionicity, melting temperature, topological freedom, density, elastic moduli), although none has been shown to describe radiation tolerance across a range of semiconductors, which exhibit a mixture of ionic and covalent bonding [8–13]. There are two main reasons why this question remains open. First, there is a lack of experimental data. While some studies exist which compare the radiation tolerance of 2 or 3 semiconductors under similar conditions, literature does not contain a relative comparison of the radiation tolerance of a substantial set of diverse semiconductors [5–7,14]. Second, all studies have searched for correlations among bulk material properties. Given that the radiation damage cascade formation and recovery depends

on the local crystal environment, it stands to reason that a fundamental, local quantity would be best able to describe radiation tolerance. This work attempts to resolve both problems by comparing the displaced lattice atom buildup rate [measured with Rutherford backscatter channeling (RBS/C)] in a set of seven ionic-covalent materials and using density-functional-theory-derived electron-density-based [processed within the quantum theory of atoms in molecules (QTAIM)] parameters to find correlations with the experimentally derived tolerance to the introduction of radiation-induced lattice defects.

According to the generalized Hellmann-Feynman equation, the force exerted on a fixed nucleus in a system of nuclei and electrons is the classical electrostatic attraction exerted by other nuclei and the electron charge density distribution for all electrons. The implication of this equation is that the electron density distribution and positions and charges of nuclei are potentially useful predictors of the ability of displaced atoms to recover perfect crystallinity following radiation-induced displacement as they determine the forces at work [15]. The Hellmann-Feynman equation is the antecedent of the Hohenberg-Kohn theorem, which builds on the claim of the fundamental importance of the electron density by showing that the electronic density determines all properties of a system of nuclei and electrons. While this may appear to be an oversimplification as such forces as exchange (electrons must be indistinguishable) and Pauli repulsion (electron wave functions must be antisymmetric) are not treated, this is not the case because these forces are not true physical forces but rather terms required for the Schrödinger equation to yield a good approximate solution. Schrödinger himself was careful to emphasize that the wave function has no physical significance while the electron density is a true physical observable as both electronic orbitals and their overlaps are mathematical constructs [16]. This being the case, the electron density distribution is used in the work to attempt to find correlation with the ability of displaced lattice atoms to recover their ideal crystal positions.

The electron density distribution $\rho(\mathbf{r})$ is a probability distribution that quantifies the average electronic charge arrangement in real space. The principal topological features of this distribution are the local maxima at nuclear attractors, which usually occur at nuclear positions. Critical points in this distribution can be defined as points where all components of the gradient of the density are equal to zero. As the gradient is a vector field which points in the direction of steepest increase, these critical points can be distinguished by their second derivative as local minima, local maxima, and saddle points (the latter two being situated on interatomic surfaces). The sign of this Laplacian is informative. If it is positive, it is an indication of locally depleted electron density or an expansion relative to the average (Lewis acid, electron acceptor). On the other hand, if it is negative, it is indicative of a Lewis base where electron density is locally concentrated, electrons are tightly bound, and the electron density is compressed relative to the average. This will form a shell structure of depleted and concentrated layers for an isolated atom, with the outer concentration shell representing the valence shell charge concentration. When bonding occurs, these shells are no longer spherical.

This topological analysis further permits definition of bond paths [17]. These bond paths represent a local maximum electron density line which links two nuclei. There is a local minimum electron density along this line which represents the bond critical point (BCP) and coincides with the point at which the bond path intersects the zero-flux $\rho(\mathbf{r})$ surface separating the atomic basins. As such, two $\rho(\mathbf{r})$ trajectories begin on the BCP and end on the nuclear attractors participating in the bond. The BCP exists any time that two attractors are separated by an interatomic zero-flux surface. The BCP is the point where the bond path intersects the zero-flux surface. These bond paths are mirrored by lines representing the maximum negative potential energy in the crystal. These are referred to as virial paths and represent lines of maximum stability in real space. The virial field and the electron density are homeomorphic. In summary, bonded nuclei share a common interatomic zero-flux surface and BCP and are connected by a bond path or equivalently, a virial path.

II. METHODS

A. Rutherford backscatter channeling

The Cambridge Laboratory for Accelerator Surface Science (CLASS) General Ionex 1.7 MV tandem ion accelerator, or Tandetron, is used for RBS/C experiments with the Alphatross RF plasma source used to generate the He beam. The damage is done with a 20 keV He^- beam (25 nA current) to ensure that damage is done in a depth range visible with the probe beam (electronic and nuclear stopping power as a function of depth given in Fig. S12 in Ref. [18]), also see Ref. [19]. Ideally to assess fitness for operation in space, one would induce damage with the same particle distribution (type and energy) as the component would be subject to in the particular earth orbit anticipated. Typically, high-energy (>50 MeV) protons are used, although we have previously shown that lower energy protons provide a more representative ratio of nuclear to electronic energy deposition to that incurred by the total radiation environment in orbit [20]. This being the case, the particles used here while certainly not the same as those seen in orbit, do not do a worse job at approximating the damage done in orbit than do typical radiation tolerance characterizations. The RBS/C characterization is done with a 1 MeV He^+ beam (2 nA current). The damage beam passes through 3-mm and 2-mm apertures while the probe beam passes through an additional 1-mm aperture to ensure that only the damaged region is probed and to ensure minimal beam divergence incident upon the sample (to maximize channeling).

The planned doses for this experiment were 1×10^{14}, 5×10^{14}, 2×10^{15}, 8×10^{15}, and 6×10^{16} He/cm^2, but after conducting this process for Si it was determined that more linear spacing at the higher doses is desirable. As a result, the following doses are employed for all subsequent materials: 5×10^{14}, 2×10^{15}, 1×10^{16}, 3×10^{16}, and 6×10^{16} He/cm^2. This resulted in seven spectra collected per material: preradiation, five as a function of damage, and a final spectrum taken with the sample pushed out of alignment ($7°$ rotation in ϕ) to provide a reference amorphous spectrum to be used in the calculation of $\Delta\chi_{min}$, which is the difference in backscatter yield

of the damaged and perfect spectra divided by the backscatter yield of the randomly oriented spectrum as a function of energy or

$$\Delta \chi_{\min} = \frac{Y^{\text{damaged}}(z) - Y^{\text{perfect}}(z)}{Y^{\text{random}}(z)}. \qquad (1)$$

$\Delta \chi_{\min}$ is used in the calculation of defect fractions for all materials except for GaP, which accumulated defects very rapidly even from the initial alignment leading to a use of $\chi_{\min}$, which is the same as $\Delta \chi_{\min}$ except that it does not include the subtraction of the $Y^{\text{perfect}}(z)$ (which will have a larger backscatter than the perfect sample due to the accumulation of defects from the alignment). The GaP sample exhibited a visible black spot from the damage beam on the sample surface from as low a dose of 90 nC. Each sample is taken out of the channeling configuration during the damage and placed back into the channeling configuration for data acquisition in each cycle. Data analysis is conducted using the Dechanneling in crystals and defect analysis (DICADA) code, which has as its starting point Lindhard's framework for atomic channeling, which treats the crystal as parallel strings of atoms. The code incorporates material constituents, crystal lattice, temperature, and experimental detection parameters [21].

Analog electronics are used to determine when channeling is achieved as well as to collect the energy spectra of backscattered He ions. The detector used in this analysis is an Ametek C-021-300-100, which is an annular partially depleted silicon surface barrier detector. It has a total area of 300 mm^2 (including the 4 mm diameter hole) and a guaranteed maximum resolution of 21 keV for alpha particles. It has a minimum depletion depth of 100 μm and is operated at +70 V. It is placed at 180° from the sample (with the incident beam passing through the open center of the annular detector). The output from this detector, consisting of voltage pulses for each He ion detected, is fed into a preamplifier and then into an amplifier (gain setting of 500 000 and shaping time of 0.5 μs). From there, the signal is fed into a multichannel analyzer as well as a count rate meter single channel analyzer (SCA ORTEC 550A) followed by a rate meter (ORTEC 541). The former is used to collect the spectra. The latter is used to assess the quality of the channeling, with the best channeling configuration resulting in minimum backscatter yield into the detector and registered in the rate meter's analog display. To achieve channeling, both sample stage degrees of freedom are simultaneously, manually adjusted until a minimum in the count rate meter is achieved. The SCA is employed in integral mode and the lower level is adjusted to cut out the low-energy noise and increase the sensitivity to distinguish the optimal channeling configuration. This is achieved by assessing the count rate with the detector biased and the beamline Faraday cup closed.

During spectrum acquisition, the total charge of incident He$^+$ ions incident on the target is registered to ensure that the spectra are collected for constant incident number of particles. The BNC lead connected to the sample stage is connected to a timer counter unit to collect a total of 1 μC (Ortec 773). Once this total charge is achieved, the Faraday cup is manually closed and the true total charge recorded (usually slightly over 1 μC) to permit precise renormalization and fitting.

A range of readily accessible wafers were selected for analysis. When available, n-type substrates were chosen with the intention of maximizing the likelihood that defects are negative or neutrally charged, in order to trap positrons in a positron annihilation lifetime experiment that was being performed in parallel (manuscript in progress). All were selected to be of thickness of at least 350 μm. GaN was grown via hydride vapour phase epitaxy with Ge doping and a minimum carrier concentration of 1×10^{18} cm^{-3}. MgO was gown via arc melting. Both GaN and MgO were sourced from MSE Supplies LLC. ZnO was grown through a hydrothermal method. GaP was grown through the Czochralski method with S doping and a minimum carrier concentration of 2.5×10^{17} cm^{-3}. InAs was grown through the Liquid Encapsulated Czochralski process and was S doped with a minimum carrier concentration of 1×10^{17} cm^{-3}. InP was grown through a Vertical gradient freeze process and was S doped with a minimum carrier concentration of 1.7×10^{18} cm^{-3}. Si was grown through a Czochralski process and was As doped with a minimum carrier concentration of 1×10^{18} cm^{-3}. ZnO, GaP, InAs, InP, and Si were sourced from MTI Corporation.

B. Density functional theory

For all elements, the pseudopotential files recommended explicitly by the Vienna *ab initio* simulation package (VASP) are employed. These are the projector augmented-wave (PAW) potentials which are more accurate than ultrasoft pseudopotentials due to their smaller core radii and their ability to precisely build up the exact valence wave function with all nodes in the core region [22]. Under this umbrella, the *GW* variants are employed, as recommended by VASP developers. These are at least as good as the DFT standard potentials and offer superior performance for excited state properties [23]. VASP offers further variability with -d indicating that semicore d electrons are treated as valence and -sv indicating that semicore s states are treated as valence. For first row elements, there are standard and -s variants. The former is highly accurate while the latter is significantly softer and is not recommended. With this in mind, the following pseudopotential files recommended by VASP are employed in this effort: PAW N_GW 10Apr2007, PAW P_GW 19Mar2012, PAW O_GW 28Sep2005, PAW As_GW 20Mar2012, PAW Si_GW 04May2012, PAW Zn_sv_GW 01Dec2010, PAW Mg_sv_GW 20Apr2010, PAW Ga_d_GW 06Jul2010, and PAW In_d_GW 29May2007. Incorporation of semicore electrons into the valence helps to reduce errors associated with the frozen core approximation [24].

The HSE-06 (Heyd-Scuseria-Ernzerhof) range-separated hybrid functional, which sits on the highest-accuracy rung on the ladder of functionals, is employed. All simulations are performed with spin polarization and spin-orbit coupling. The initial magnetic moment for each atom is treated as equal to 0.6 times the number of atoms in the simulation [25].

The starting point for atomic positions is the POSCAR file obtained from the converged Materials Project DFT simulations, from which the atomic positions, cell shape, and cell volume are all allowed to vary freely in subsequent relaxation. This is performed as a function of energy cutoff and k-point grid discretization. Given that a HF/DFT hybrid functional

is used, VASP recommends use of a direct optimization algorithm. The VASP Damped algorithm is found to be sufficient for all semiconductors analyzed in this effort except for MgO, for which the VASP All algorithm was required to achieve convergence.

In order to output all of the requisite files to conduct a complete QTAIM analysis, a few flags must to set in VASP. Specifically, one needs the individual all-electron charge densities on the fine FFT grid AECCAR0, AECCAR1, and AECCAR2 which contain, respectively, the core density, proto-atomic valence density (overlapping atomic charge densities), and the self-consistent valence density. The first two are defined at the input of the run and do not change as convergence is approached. In comparison, the latter one AECCAR2, contains the final self-consistent valence electron density. This all-electron density is rapidly varying near the nuclei and is typically costly to expand into plane waves, but this expansion is done to output AECCAR2. The primary field under analysis in determination of critical points within QTAIM is composed of the sum of the AECCAR0 and AECCAR2 fields as it will properly contain maxima in the electron density. However, for integration within atomic basins, CHGCAR is used.

For all systems, an electronic stopping criterion of 1×10^{-5} eV is chosen. This value defines the termination of the electronic system degree of freedom relaxation. When the total free energy change and the band-structure-energy change between two relaxation steps falls below this value, electronic convergence is defined to be achieved [23]. In terms of E_{cut} and k-point grid density convergence, convergence is defined in this effort where the difference in successive simulation total free energy of the ion-electron system falls below 0.05 eV.

III. RESULTS

The materials analyzed are InAs, InP, GaN, GaP, ZnO, MgO, and Si. The materials chosen for analysis are selected to have diversity in electron density spatial distributions [$\rho(\mathbf{r})$]. This distribution is of fundamental importance given that the Hellmann-Feynman theorem states that the electron density distribution and positions and charges of nuclei describe the forces felt by atoms and their bonding [15]. Associated with this, another material selection criterion was the fractional ionic/covalent bonding (ionicities).

A. Rutherford backscatter channeling experimental radiation tolerance

RBS/C is used to assess the rate of displaced lattice atom accumulation as a function of dose in the materials analyzed. This structural characterization method is independent of the carrier concentrations and dynamics and allows comparison of damage accumulation across a diverse set of materials. An accelerator He ion beam is aligned with channels in the single crystal samples and the backscattered ion energy spectrum is measured and associated with depth into the material. This backscattered ion yield increases in magnitude and varies in structure as atoms are displaced into interstitial sites in the crystal channel due to radiation-induced lattice damage.

The preradiation spectrum will consist of ions backscattered due to initial mis-alignment with crystal channels and dechanneling of ions due to interaction with vibrating lattice atoms, electrons, and native displaced lattice atoms. Increase in yield at the lowest energies also results from detector noise. The high-energy cutoff of these spectra is determined by kinematics, with the highest energy backscattered ions resulting from backscatter events from the heaviest elements near the surface of the sample. As energy in the spectrum decreases, ions backscattered from deeper into the material contribute to the spectra. One can also probe the spectrum obtained by mis-aligning the incident ion beam. The resulting spectrum is representative of the spectrum obtained from an amorphous material.

With increasing displacement damage from radiation dose, accumulating lattice atoms will be sufficiently displaced into crystal channels to induce incident ion dechanneling and backscatter through ion Coulombic interaction with these displaced lattice atoms. These increasing backscattered ions will primarily result from the shallow depth over which the 20 keV He$^-$ beam damages the material. This occurs in the high-energy regime because ions backscattered from this region have lost little energy in being transmitted through the material. The calibrated, backscattered 1 MeV He$^+$ spectra are plotted in Fig. 1, normalized by the number of He$^+$ probe ions incident upon the sample in spectrum acquisition (approximately 1 μC). In these plots is shown the predamage spectrum, the spectrum as a function of dose (20 keV He$^-$), and the unaligned spectrum which is characteristic of an amorphous lattice of the constituent elements. The increase in backscatter yield with dose is apparent in all materials.

The slope of the integrated backscattered spectra as a function of dose provides a measure of defect accumulation rate, although such a simple analysis would fail to include differences in crystal structure and charge density among the materials characterized. Instead, these channeled spectra are analyzed by solving the master equation describing the energy of incident ions in a direction perpendicular to the channel $E_\perp$ as a function of depth into the material, as altered by interactions [21]. Instead of treating the distribution of $E_\perp$ as a function of depth $g(E_{perp}, z)$ as a continuous distribution, it can be treated as a system of differential equations (master equation) as

$$\frac{dg_i(z)}{dz} = \sum_j [P_{ij}g_j(z) - P_{ji}g_i(z)] = \sum_j Q_{ij}g_j(z), \quad (2)$$

in which $g_i(z)$ is the relative number of ions with transverse energy in bin i as a function of depth and P_{ij} is the probability per unit depth of transition from transverse energy interval j to i. Q_{ij} is the dechanneling matrix, which contains all information about the dechanneling processes. It represents the sum of three contributions: interactions with (1) electrons, (2) thermal vibrations, and (3) displaced lattice atoms [21]. Solving this equation yields the displaced lattice atom concentration as a function of depth into the material. It should be emphasized that this analysis assumes uncorrelated defects and provides the total concentration of atoms with sufficient displacement into the channels to induce incident ion dechanneling. This value exceeds the individual point defect and extended defect
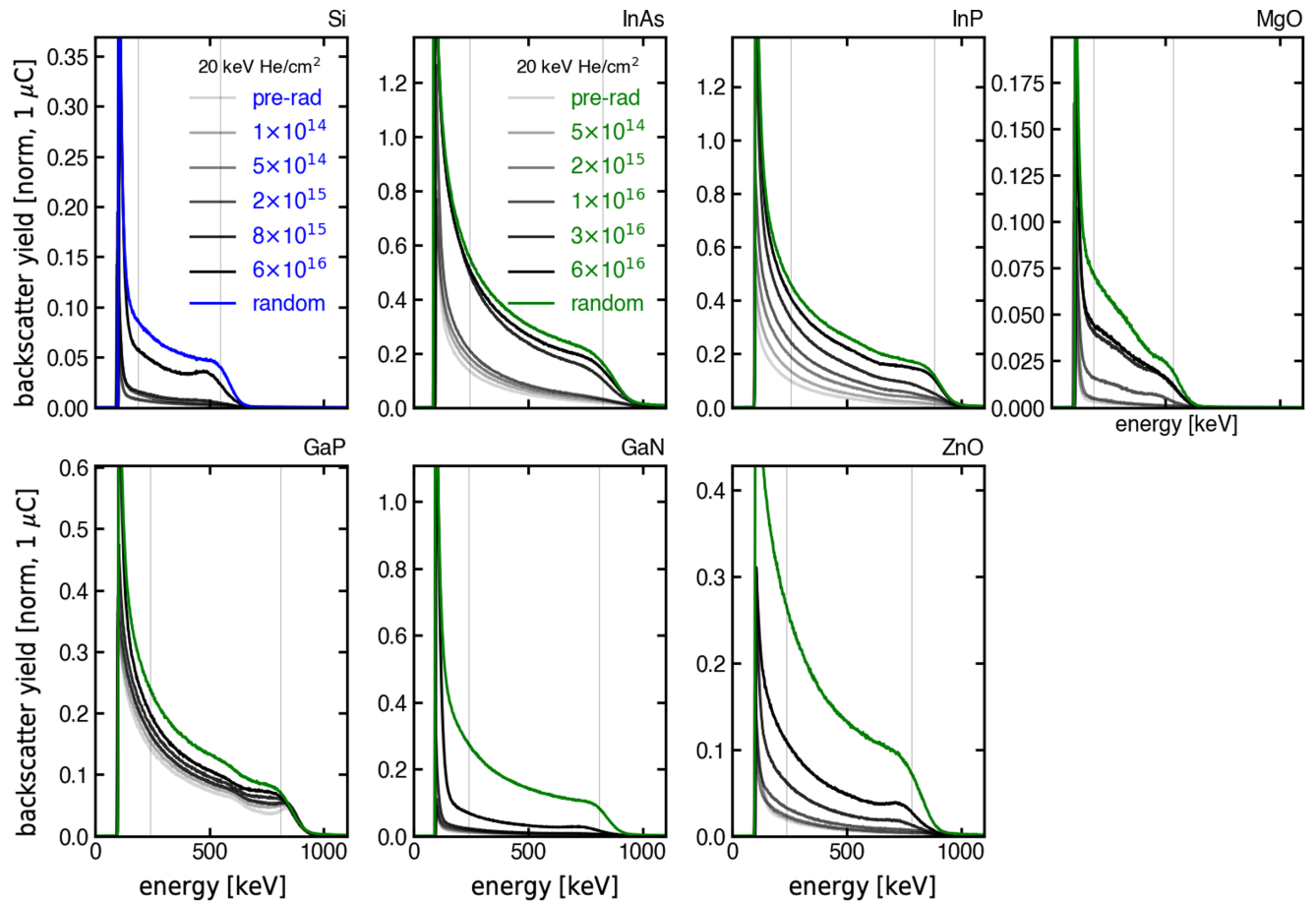
FIG. 1. Backscattered 1 MeV He$^+$ probe beam ion yield as a function of 20 keV He$^-$ ion dose alongside the dechanneled (random) spectra for each material examined. Increasing dose is indicated by increasing line saturation with the doses for Si and InAs labeled and all unlabeled spectra having the same doses as InAs. The backscattered yield is shown to increase consistently with dose.

concentrations due to their associated strain fields, with extended defects being associated with large strain fields capable of inducing dechanneling (as discussed in Ref. [18]) [26–28]. The resulting fitted displaced lattice atom concentrations as a function of dose are shown in Fig. 2 as a function of depth with the green and blue lines indicating the normalized defect production as a function of depth as predicted by SRIM [19].

GaP, InP, InAs, MgO, and Si all exhibit large defect fractions in the damaged region, while the values are smaller for GaN and ZnO. All materials exhibit substantial defect fractions beyond the damage zone as predicted by SRIM. This is to be anticipated because the diffusion of interstitials in semiconductors can easily exceed 1 μm, especially under irradiation [29].

The parameter of primary interest in this analysis is the relative displaced atom accumulation rate in these materials, which is derived from the integral of Fig. 2 (with a fit associated with the solution to the point defect diffusion equation to obtain total displaced lattice atom fractions beyond the range probed with RBS/C). The final displaced lattice atom number per unit area in each material as a function of dose is show in Fig. 3. It is observed that GaN exhibits the lowest defect accumulation rate, closely followed by ZnO. InAs exhibits a similar defect buildup rate at the lower doses but exhibits a higher defect accumulation rate at the higher doses. Si and InP

have a higher defect accumulation rate that is similar. GaP has the next highest point defect buildup rate[1] and MgO has the highest. This ranking in material tolerance to buildup of displaced lattice atoms under radiation damage is compared with local material properties to obtain a fundamental link between material properties and displaced lattice atom accumulation.

B. Quantum theory of atoms in molecules assessment of density functional theory results and comparison to experimental relative radiation tolerance

Electron density distributions are obtained from hybrid density functional theory simulations. These total electron densities (core and valence) are post-processed within the Quantum Theory of Atoms in Molecules (QTAIM), which assesses the gradient and Laplacian of the electron distribution to identify critical points in the crystal lattice and atomic basins (which are rigorously defined to obey the hypervirial and virial theorems) [30]. Critical points represent points of zero electron density gradient [$d\rho(\mathbf{r})/dx = 0$, $d\rho(\mathbf{r})/dy = 0$,

---

[1]GaP accumulated defects rapidly under the minimal, unavoidable initial alignment dose of 90 nC. This was observed in no other materials.
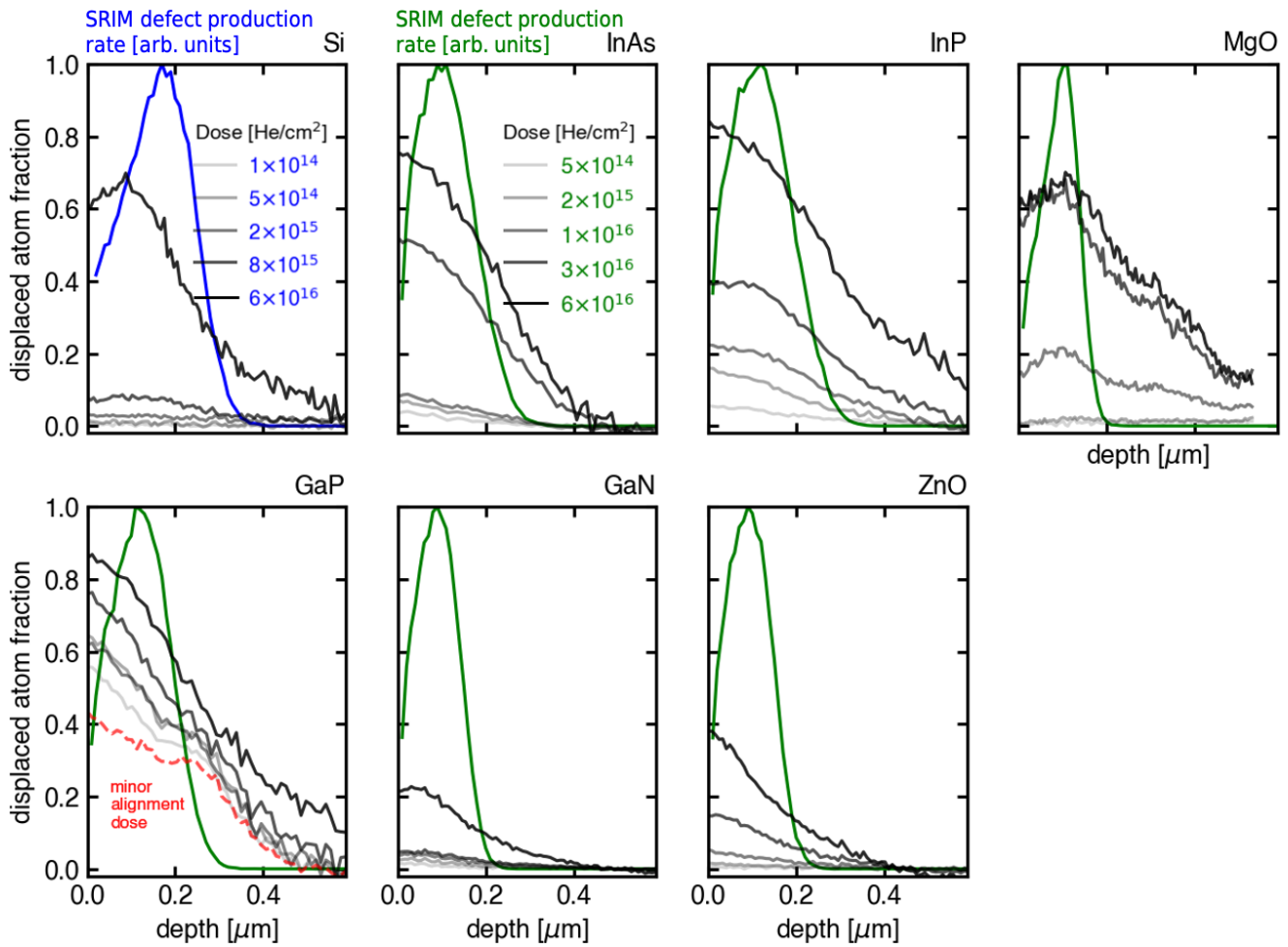
FIG. 2. Fraction of displaced lattice atoms as a function of depth obtained by fitting the Rutherford backscatter channeling spectra in Fig. 1. The blue and green lines are the normalized defect production rate as a function of depth as predicted by SRIM. Increasing dose is indicated by increasing line saturation with the doses for Si and InAs labeled and all unlabeled spectra having the same doses as InAs. The defect concentration is shown to increase consistently with dose. These concentrations are larger than the lattice could sustain if they all constituted point defects. The fitted displaced lattice atom concentration includes the atoms sufficiently displaced into channels by the strain fields of point defects (as discussed in Ref. [18]) and also extended defects, which induce dechanneling very efficiently [26].

and $d\rho(\mathbf{r})/dz = 0$] and indicate the position of attractors (maxima), bonds (first-order saddle points), rings (second-order saddle points), and cages (minima). Little differentiation of materials is found among the number and multiplicity of each type of critical point, as they are mainly determined by the crystal structure. An exception exists for the ring critical points for which all materials except for MgO and Si have a number of ring critical points equal to the number of bonds. For MgO and Si, a much larger number of ring critical points is identified (144 and 112, respectively). These ring critical points are not indications of crystal defects but are rather topological features in the electron density. They represent second-order saddle points in the electron density and a large number of ring critical points is indicative of a rapidly changing electron density to require this large number of saddle points.

In addition to the number of critical points, their properties can also be analyzed. The geometry of bond critical points is highlighted here due to its potential relationship to radia-

tion tolerance. These properties are shown in Fig. 4, with a horizontal axis logarithmically spaced with the total accumulation of displaced lattice atoms according to RBS/C. For all bond critical points, the geometric distance between the bond critical point and the nuclear attractor critical points which it connects are shown in Fig. 4(a) (the straight-line distance between critical points within the unit cell). It is observed that these distances are smaller in ZnO and GaN while MgO shows considerable spread in these distances, with some distances being large. InP, GaP, Si, and InAs all exhibit large distances. Figure 4(b) shows the ratio of the distances on either side of the bond critical point to the adjacent nuclear attractors (cation distance divided by anion distance). A value far from unity indicates that the bond critical point is biased toward one of the bonded atoms and is an indicator of polarization of the bond. InP, ZnO, and GaN exhibit a moderate bias. Si and InAs indicate minimal bias. One MgO bond indicates minimal bias with the other bias being extreme and GaP exhibits an extreme bias in all bonds. Figure 4(c) shows the angle formed
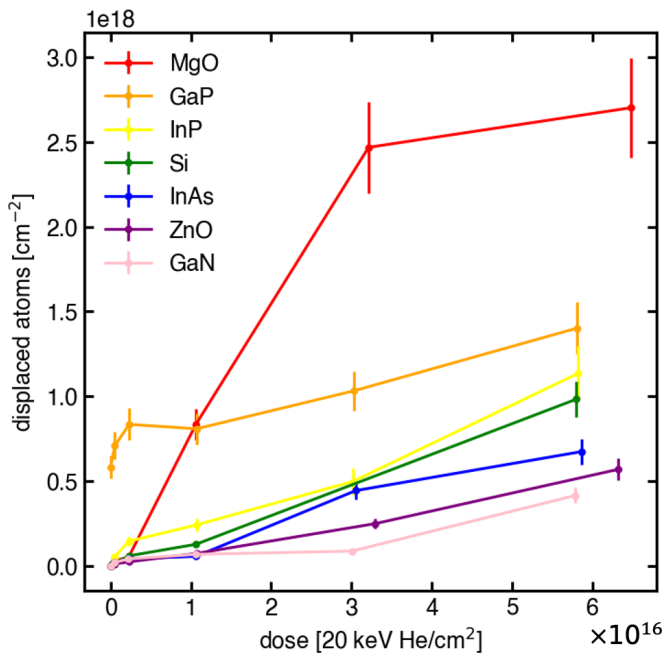
FIG. 3. Integrated displaced lattice atom concentration introduced as a function of dose for all materials (based on integrating Fig. 2). These numbers are larger than the lattice could sustain if they all constituted point defects. They include the atoms sufficiently displaced into channels by the strain fields of point defects (as discussed in Ref. [18]) and also extended defects, which induce dechanneling very efficiently [26].

by the lines connecting the bond critical point and the bonded nuclei. All bond angles except for InAs are almost entirely linear (bond critical point is not offset from the straight line connecting the bonded atoms). Finally, the total bond path length is shown in Fig. 4(d) [sum of bond values in Fig. 4(a)]. ZnO and GaN show shorter bond path lengths while InAs, Si, GaP, and InP show larger path lengths. MgO exhibits both short and long path lengths. The shorter path length could be indicative of a stronger bond and perhaps increased radiation tolerance, although such a simple structural correlation has not proved successful in previous work [8,9].

Further quantities can be analyzed at the critical points in all materials, with the bond critical points having particular significance as the stabilizing interaction [31]. The eigenvalues of the Hessian matrix of the total electron density and derived quantities are shown in Fig. 5. The three eigenvalues themselves are shown in Fig. 5(a). Bond critical points by definition have one positive eigenvalue (indicating local electron depletion at the bond critical point along the bond path direction) and two negative eigenvalues (indicating local electron accumulation along the bond path in directions perpendicular to the bond path). The magnitude of the eigenvalues themselves indicates the strength of this accumulation or depletion. These values can more generally be interpreted as the strength of the curvature with the sign of the eigenvalue indicating the direction of the curvature; positive along the bond path (upward toward the bonded atoms) and negative perpendicular to the bond path (downward away from the bond path).

Considering the positive eigenvalues in Fig. 5(a), it is observed that GaN and ZnO have strong local electron depletion along the bond path at the bond critical point, potentially indicating a more ionic bond and also little barrier to defect migration and potential recovery due to the fact that the electrons present are strongly associated with the bonded atoms, making them less available to form a bond with the defective interstitial atom. This steep slope toward the bonded atoms could encourage further interstitial atom diffusion and eventual recovery. MgO shows strong depletion at some bond critical points and weak depletion at others, indicating that some recovery pathways have impediments and some do not. InP, GaP, and InAs all exhibit moderate to weak depletion along the bond path at the bond critical point and Si exhibits minimal depletion. This could represent the potential of the migrating interstitial atom to obtain a stable position at these defective points in the crystal. Considering the negative eigenvalues, ZnO and GaN have the strongest electron accumulation relative to the region perpendicular to the bond with all other materials exhibiting approximately equivalent weak accumulation. The relative flatness of the electron density in these materials could represent a potential point of localization of the diffusing defective interstitial atom. The magnitude of the eigenvalues at bond critical points is an indicator of the curvature of electron density at the critical point. This sum in quadrature, indicating the effective divergence from flatness (degree of curvature), is given in Fig. 5(b). It is observed that ZnO and GaN have by far the strongest curvature of electron density near the critical point. This could indicate strong driving forces for defective atoms to move away from these bonding critical points, where they may become trapped in defective states if these forces are insufficiently strong to drive them away. In comparison, GaP, InP, and InAs all exhibit much smaller curvature of electron density at these points. MgO exhibits some bonds with very low values and Si also displays smaller overall curvature. These could indicate that defective atoms are less driven away from these important material points and may become trapped. Another measure of net curvature is given in Fig. 5(c), with the results similar to those in Fig. 5(b). Due to the importance of the directionality, it is argued here that Fig. 5(a) is of more utility as the positive eigenvalues (λ_1) represent the upward curvature toward the nuclear attractors along the bond path (representing a hill to climb if bonding is to be achieved) and downward curvature (λ_2 and λ_3) perpendicular the bond path in either direction pushing the displaced lattice atom away from this key bonding site. A similar benefit of considering the individual eigenvalues over the Laplacian or other net quantities has been observed in the field of computer vision [32].

One would ideally compare these experimental results and the proposed theory with other sets of irradiated semiconductors exposed to the same radiation damage conditions, but this data is absent from the literature. Such a large-scale comparison would be excellent future work, although the characterization method must be chosen carefully to ensure that the material comparison is valid. There have been previously proposed material radiation tolerance predictors such as ratio of cation radii (observed in a subset of oxides, but not found to be applicable to our irradiated semiconductors) [33,34], crystal structure (with more close-packed crystal
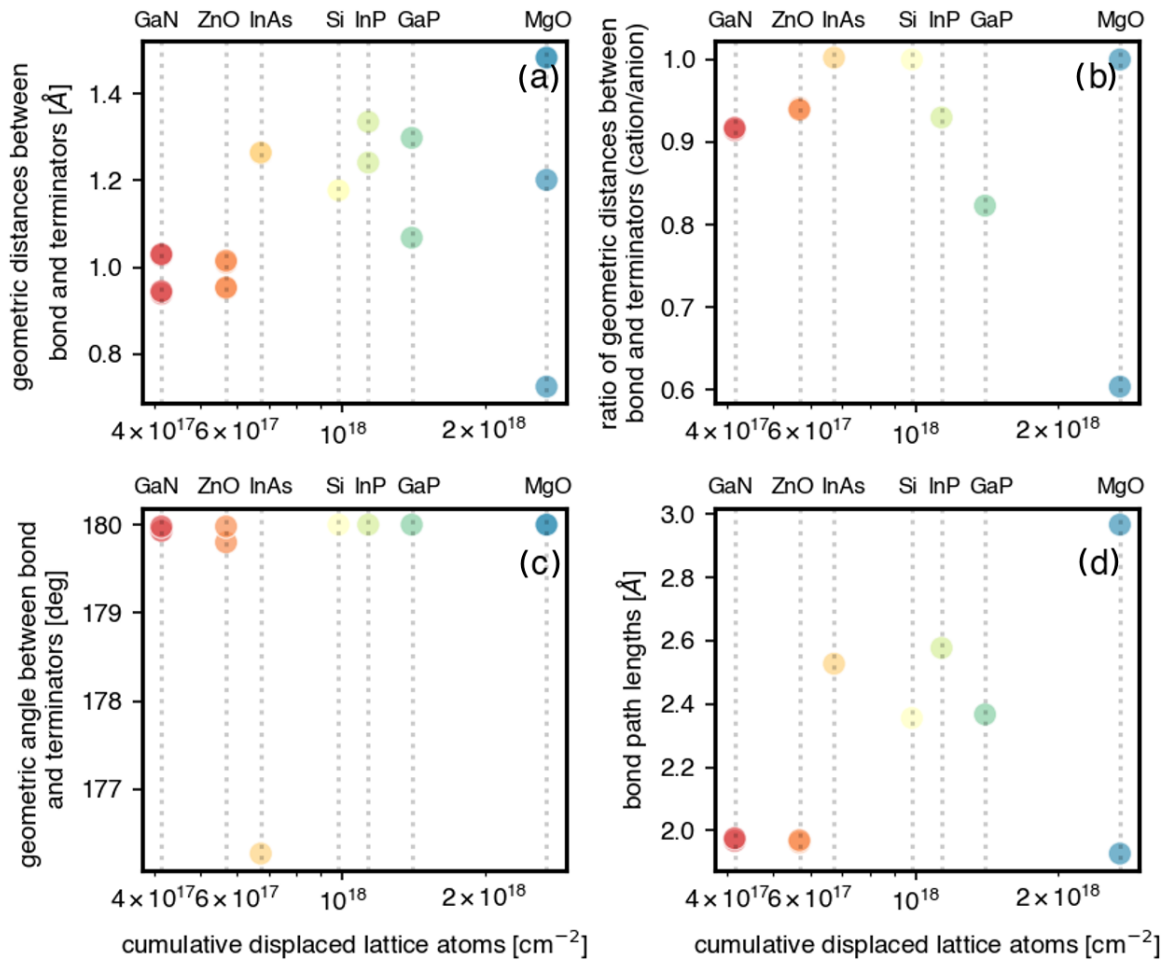
FIG. 4. Geometric information for all bond critical points in all materials. Shown are the (a) geometric distance between the bond critical point and the nuclear terminators, (b) ratio of the values for each bond shown in (a), (c) angle between the bond critical point and the terminators, and (d) the total bond path length [sum of values for each bond shown in (a)]. These figures are plotted with a horizontal axis logarithmically spaced with the cumulative displaced lattice atom concentration according to Rutherford backscatter channeling.
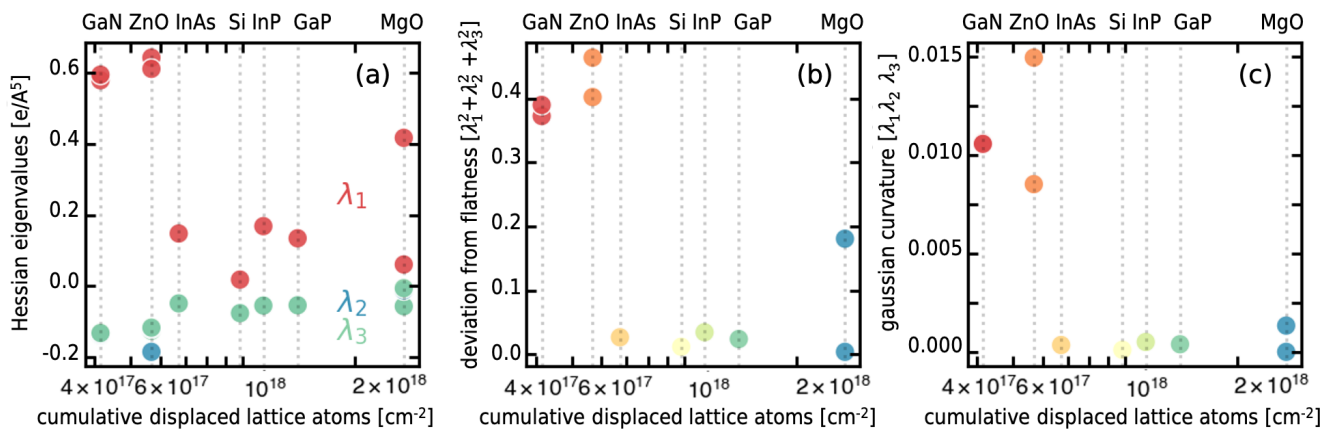

FIG. 5. Eigenvalues and derived quantities for all materials analyzed. (a) Eigenvalues of the electron density Hessian matrix (two negative perpendicular to the bond path and one positive along the bond path, indicating degree of curvature of the electron density in each direction), (b) deviation from flatness (quantified as the sum in quadrature of the eigenvalues, measure of net curvature of the electron density at the bond critical point). and (c) Gaussian curvature (another measure of deviation from flatness). These figures are plotted with a horizontal axis logarithmically spaced with the cumulative displaced lattice atom concentration according to Rutherford backscatter channeling.

structures like the wurtzite crystal structure being more radiation tolerant than the diamond crystal structure, which is in agreement with the data presented here but fails to capture the fundamental determinant and also does not distinguish semiconductors of the same crystal structure as bond distance was not found to predict radiation tolerance) [10,35], bond energy (shown for AlGaN and InGaN but proved not to be universal due to the strong radiation tolerance of HgCdTe but low bond strength) [11–13], and ratio of electronic to nuclear stopping (with electronic energy deposition improving defect mobility and annealing, but shown not to be applicable to the semiconductors studied here in Fig. S5 in Ref. [18] where the two least radiation tolerant materials are among the top three materials in terms of this ratio) [36,37]. Some more general bulk properties have been correlated with radiation tolerance, which are plotted with the horizontal axis of displaced lattice atom buildup rate as predicted by RBS/C in Fig. S4 in Ref. [18], see also Refs. [8–10,38,39]. It is observed that none of these bulk properties have a strong, universal correlation with radiation tolerance as is observed in the curvature of electron density at bond critical points. There does appear an interesting correlation between higher density and higher radiation tolerance, although the low density of silicon disproves the universality of the correlation. In general, one may hypothesize that higher density results in higher curvature of the electron density due to the heavier atoms, but this is not universally true due to the fact that Si does not disprove the electron density curvature at bond critical points trend. As such, it is proposed that the curvature of electron density at bond critical points is the more fundamental predictor.

IV. CONCLUSION

The experimental results in relative radiation tolerance of a diverse set of ionic-covalent materials as measured by RBS/C indicate that the relative buildup rate of displaced lattice atoms as a function of 20 keV He$^-$ damage is given (from most rapid buildup to slowest buildup): MgO, GaP, InP, Si, InAs, ZnO, and GaN. These experimental results are used to understand which quantum-mechanical predictive parameters correlate well with resistance to the buildup of radiation-induced defects. The predictive parameters are obtained by analyzing the electron density, its gradient, and its Laplacian in each of these materials. Previous correlations with various bulk material

parameters fail to explain the radiation tolerance observed in this effort [8–10,38], as shown in Fig. S4 in Ref. [18]. In considering the Hessian eigenvalues of the electron density, which indicate the curvature along and perpendicular to a bond point, one observes consistent trends with more radiation tolerant materials exhibiting more extreme positive eigenvalues (curvature providing a barrier in the direction of the bonded atoms) and negative eigenvalues (curvature providing a driving force away from the bond point) than less radiation tolerant materials. This can be interpreted in terms of large rates of change at these bond critical points acting as driving forces here which destabilize an atom which could otherwise form a stable defect complex at these important points in the crystal. It is observed that the electron density (typically a good indicator of bond strength) and energy values themselves are not indicators of radiation tolerance when quantified at the bond critical points (as shown in Supplemental Material [18]). Instead, the gradient and Laplacian (especially the Laplacian of the kinetic and potential energies) can predict radiation tolerance well, further illustrating the importance of considering curvature when considering radiation tolerance. This importance of considering curvature is further illustrated by considering a plot of the gradient of the electron density with respect to an indicator of bond strength and character (Fig. S3 in Ref. [18]). It is observed that the most radiation-resistant materials exhibit strong dispersion in these values, indicating rapidly transitioning quantities to enable this diversity. In comparison, MgO, InP, GaP, and Si all have more tightly distributed values, indicating more uniformity overall in the unit cell and potential defect locations of stability. As such, the ultimate conclusion is that radiation tolerance is enhanced by the existence of rapidly changing, high curvature electron density at bond critical points in the crystal structure. Bulk material quantities are unable to capture this information.

---

[1] L. Novikov, V. Mileev, E. Voronina, L. Galanina, A. Makletsov, and V. Sinolits, Radiation effects on spacecraft materials, J. Synch. Investig. **3**, 199 (2009).

[2] G. D. Jenkins, C. P. Morath, and V. M. Cowan, Empirical study of the disparity in radiation tolerance of the minority-carrier lifetime between II–VI and III–V MWIR detector technologies for space applications, J. Electron. Mater. **46**, 5405 (2017).

[3] F. Tuomisto, V. Ranki, K. Saarinen, and D. C. Look, Evidence of the Zn Vacancy Acting as the Dominant Acceptor in *n*-type ZnO, Phys. Rev. Lett. **91**, 205502 (2003).

[4] J. Silc, B. Robic, and T. Ungerer, *Processor Architecture - From Dataflow to Superscalar and Beyond* (Springer, Verlag, Berlin, Heidelberg, 1999), p. 34.

[5] T. Markvart, Radiation damage in solar cells, J. Mater. Sci.: Mater. Electron. **1**, 1 (1990).

[6] E. Wendler, W. Wesch, A. Azarov, N. Catarino, A. Redondo-Cubero, E. Alves, and K. Lorenz, Comparison of low- and room-temperature damage formation in Ar ion implanted GaN and ZnO, Nucl. Instrum. Methods Phys. Res., Sect. B **307**, 394 (2013).

[7] P. Partyka, R. S. Averback, D. V. Forbes, J. J. Coleman, and P. Ehrhart, X-ray diffraction and channeling-Rutherford

backscattering spectrometry studies of ion implantation damage in $Al_xGa_{1-x}As$, J. Appl. Phys. **83**, 1265 (1998).

[8] R. K. Eby, R. C. Ewing, and R. C. Birtcher, The amorphization of complex silicates by ion-beam irradiation, J. Mater. Res. **7**, 3080 (1992).

[9] R. Ewing, L. Wang, and W. Weber, Amorphization of complex ceramics by heavy-particle irradiations, MRS Proceedings **373**, 347 (1994).

[10] K. Nordlund, M. Ghaly, R. S. Averback, M. Caturla, T. Diaz de la Rubia, and J. Tarus, Defect production in collision cascades in elemental semiconductors and FCC metals, Phys. Rev. B **57**, 7556 (1998).

[11] S. Kucheyev, J. Williams, and C. Jagadish, Ion-beam-defect processes in group-III nitrides and ZnO, Vacuum **73**, 93 (2004).

[12] H. H. Tan, C. Jagadish, J. S. Williams, J. Zou, D. J. H. Cockayne, and A. Sikorski, Ion damage buildup and amorphization processes in $Al_xGa_{1-x}As$, J. Appl. Phys. **77**, 87 (1995).

[13] A. Rogalski, HgCdTe infrared detector material: History, status and outlook, Rep. Prog. Phys. **68**, 2267 (2005).

[14] G. Dlubek, C. Ascheron, R. Krause, H. Erhard, and D. Klimm, Positron study of vacancy defects in proton and neutron irradiated GaP, InP, and Si, Phys. Stat. Sol. (a) **106**, 81 (1988).

[15] P. Politzer and J. Murray, The Hellmann-Feynman theorem: A perspective, J. Mol. Model. **24**, 266 (2018).

[16] E. Schrödinger, Quantisierung als eigenwertproblem, Ann. Phys. **384**, 361 (1926).

[17] G. Runtz, R. Bader, and R. Messer, Definition of bond paths and bond directions in terms of the molecular charge distribution, Can. J. Chem. **55**, 3040 (1977).

[18] See Supplemental Material at http://link.aps.org/supplemental/10.1103/PhysRevMaterials.6.084601 for additional QTAIM DFT analysis, additional assessment of the ability of bulk parameters to predict radiation tolerance, calculation of the efficiency of point defects in inducing dechanneling in RBS/C, and the electronic and nuclear stopping power for the damaging He ions using in the RBS/C experiment here.

[19] J. F. Ziegler, SRIM - The stopping and range of ions in matter (2013).

[20] J. Logan, M. Short, P. Webster, and C. Morath, Orbital equivalence of terrestrial radiation tolerance experiments, IEEE Trans. Nucl. Sci. **67**, 2382 (2020).

[21] Konrad Gartner, K. Hehl, and G. Schlotzhauer, Axial dechanneling: I. Perfect crystal, Nucl. Instrum. Methods Phys. Res. **216**, 275 (1983).

[22] G. Kresse and D. Joubert, From ultrasoft pseudopotentials to the projector augmented-wave method, Phys. Rev. B **59**, 1758 (1999).

[23] G. Kresse, M. Marsman, and J. Furthmüller, *VASP the GUIDE*, Computational Materials Physics, Faculty of Physics, (Universit at Wien, Wien, Austria, 2018).

[24] J. Paier, M. Marsman, K. Hummer, G. Kresse, I. C. Gerber, and J. G. Ángyán, Screened hybrid density functionals applied to solids, J. Chem. Phys. **124**, 154709 (2006).

[25] A. Jain, S. P. Ong, G. Hautier, W. Chen, W. D. Richards, S. Dacek, S. Cholia, D. Gunter, D. Skinner, G. Ceder, and K. A. Persson, The Materials Project: A materials genome approach to accelerating materials innovation, APL Mater. **1**, 011002 (2013).

[26] S. Zhang, K. Nordlund, F. Djurabekova, Y. Zhang, G. Velisa, and T. S. Wang, Simulation of Rutherford backscattering spectrometry from arbitrary atom structures, Phys. Rev. E **94**, 043319 (2016).

[27] J. Lindhard, Motion of swift charged particles, as influenced by strings of atoms in crystals, Phys. Lett. **12**, 126 (1964).

[28] E. Clouet, C. Varvenne, and T. Jourdan, Elastic modeling of point-defects and their interaction, Comput. Mater. Sci. **147**, 49 (2018).

[29] E. Schubert, *Doping in III-V Semiconductors* (MRS Online Proceedings Library, 2015), pp. 273–282.

[30] S. Srebrenik and R. F. Bader, Towards the development of the quantum mechanics of a subspace, J. Chem. Phys. **63**, 3945 (1975).

[31] H. Yang, P. Boulet, and M.-C. Record, A rapid method for analyzing the chemical bond from energy densities calculations at the bond critical point, Comput. Theor. Chem. **1178**, 112784 (2020).

[32] J. Hladuvka, A. König, and E. Gröller, Exploiting eigenvalues of the Hessian matrix for volume decimation *in Proceedings of the 9th International Conference on Computer Graphics, Visualization, and Computer Vision*, (University of West Bohemia, 2001), pp. 124–129.

[33] K. E. Sickafus, L. Minervini, R. W. Grimes, J. A. Valdez, M. Ishimaru, F. Li, K. J. McClellan, and T. Hartmann, Radiation tolerance of complex oxides, Science **289**, 748 (2000).

[34] K. E. Sickafus, L. Minervini, R. W. Grimes, J. A. Valdez, and T. Hartmann, A comparison between radiation damage accumulation in oxides with pyrochlore and fluorite structures, Radiat. Eff. Defects Solids **155**, 133 (2001).

[35] N. Chen, E. Rasch, D. Huang, E. R. Heller, and F. Gao, Atomic-scale simulation for pseudometallic defect-generation kinetics and effective NIEL in GaN, IEEE Trans. Nucl. Sci. **65**, 1108 (2018).

[36] A. Meldrum, L. A. Boatner, and R. C. Ewing, Displacive radiation effects in the monazite- and zircon-structure orthophosphates, Phys. Rev. B **56**, 13805 (1997).

[37] A. Meldrum, L. A. Boatner, and R. C. Ewing, Effects of ionizing and displacive irradiation on several perovskite-structure oxides, Nucl. Instrum. Methods Phys. Res., Sect. B **141**, 347 (1998).

[38] K. Trachenko, Understanding resistance to amorphization by radiation damage, J. Phys.: Condens. Matter **16**, R1491 (2004).

[39] W. Harrison, *Electronic Structure and the Properties of Solids: The Physics of the Chemical Bond*, Dover Books on Physics (Dover, 1989), p. 173.